

# Journal of Materials Chemistry A

Accepted Manuscript



This is an *Accepted Manuscript*, which has been through the Royal Society of Chemistry peer review process and has been accepted for publication.

*Accepted Manuscripts* are published online shortly after acceptance, before technical editing, formatting and proof reading. Using this free service, authors can make their results available to the community, in citable form, before we publish the edited article. We will replace this *Accepted Manuscript* with the edited and formatted *Advance Article* as soon as it is available.

You can find more information about *Accepted Manuscripts* in the [Information for Authors](#).

Please note that technical editing may introduce minor changes to the text and/or graphics, which may alter content. The journal's standard [Terms & Conditions](#) and the [Ethical guidelines](#) still apply. In no event shall the Royal Society of Chemistry be held responsible for any errors or omissions in this *Accepted Manuscript* or any consequences arising from the use of any information it contains.



Journal Name

ARTICLE

## High Rate Sodium Ion Battery Anodes from Block Copolymer Templated Mesoporous Nickel-Cobalt Carbonates and Oxides

Sarang M. Bhaway, Pattarasai Tangvijitsakul, Jeongwoo Lee, Mark D. Soucek, Bryan D. Vogt\*

Received 00th January 20xx,  
Accepted 00th January 20xx

DOI: 10.1039/x0xx00000x

www.rsc.org/

Micelle-templated ordered mesoporous nickel-cobalt carbonates and oxides are fabricated using a metal nitrate-citric acid strategy, which avoids the hydrolysis and aging requirements associated with sol-gel chemistry. A series of mesoporous  $\text{Ni}_x\text{Co}_{(3-x)}(\text{CO}_3)_y$  and  $\text{Ni}_x\text{Co}_{(3-x)}\text{O}_4$  films with varying Ni-Co compositions and  $14 \pm 4$  nm mesopores are fabricated with the same block copolymer template. AFM and GISAXS analysis indicates that the mesostructure is maintained through the formation of the carbonate and oxide, while GIXD profiles confirm formation of pure spinel phases of semi-crystalline  $\text{Ni}_x\text{Co}_{(3-x)}\text{O}_4$ . The micelle templated mesopores are interconnected and provide transport paths for the electrolyte to minimize the solid-state diffusion requirements associated with battery electrodes. These materials exhibit good performance as sodium ion battery anodes even at high current densities of 4 A/g. Amongst the mixed-metal oxides,  $\text{Ni}_2\text{CoO}_4$  exhibits the highest specific capacity of 239 mAh/g after galvanostatic cycling at a current density of 1 A/g for 10 cycles. We attribute the superior performance of  $\text{Ni}_2\text{CoO}_4$  at high rates to the high surface area and short ion-diffusion paths of the nanoporous anode architecture, while the higher nickel content in the mixed metal oxide provides enhanced stability to oxide towards carbonate formation along with enhanced electronic conductivity, leading to improved cycling stability of the anode. This micelle template metal nitrate-citric acid method enables new possibilities for fabricating variety of ordered mesoporous mixed-metal carbonates and oxides that could be used in a wide range of applications.

### Introduction

Soft-templating based on the cooperative assembly of block copolymers and precursors provides a convenient route to fabricate mesoporous metal oxides with precise control over pore size<sup>1</sup> and surface area.<sup>2-4</sup> These nanostructured porous materials can be applied to diverse applications, such as energy storage,<sup>5, 6</sup> gas absorption,<sup>7</sup> catalysis,<sup>8, 9</sup> and drug delivery.<sup>10</sup> For energy storage applications, the nanoscale dimensions associated with metal oxide matrix and interconnected mesopores provide short diffusion paths through the active materials and minimize ion transport issues when compared to bulk non-porous analogs.<sup>11, 12</sup> These properties can enable high capacity and cycling stability at high charge-discharge rates for templated mesoporous metal oxides electrodes in lithium ion batteries.<sup>13-15</sup>

More recently, sodium ion battery technologies have garnered interest as a low cost alternative to lithium ion

batteries.<sup>16, 17</sup> Layered (e.g., titanium oxide<sup>18</sup>) or spinel (e.g., cobalt oxide<sup>19</sup> and iron oxide<sup>20</sup>) transition metal oxides are low cost materials for negative electrodes in sodium ion batteries. However, more complex transition metal oxides, such as nickel cobaltite ( $\text{NiCo}_2\text{O}_4$ ),<sup>21</sup> enable improved theoretical performance, but the performance, especially at high discharge rate, is intimately coupled to its nanoscale architecture.<sup>22-24</sup> In this context, a wide variety of nanoscale binary metal oxides have been fabricated in the form of nanoparticles, nanoribbons and disordered mesoporous materials.<sup>22, 25, 26</sup> Ordered mesoporous structures provide an advantage of controlled transport paths, but fabrication of ordered nickel cobaltite has been generally limited to hard templating.<sup>27</sup> Although hard templating is effective, the procedure requires multiple steps and is not readily scalable for commercialization. The soft templating of highly ordered mixed metal oxides of nickel cobaltite is generally challenged by the differences in hydrolysis and condensation rates of the oxide precursors for sol-gel processing.<sup>28, 29</sup> Stucky and co-workers demonstrated that non-aqueous soft templating with metal chlorides is an effective route to generate ordered mesoporous transition metal oxides including binary and ternary metal oxides.<sup>2</sup> However, the long aging time (~ 2 days) significantly limits the commercial potential due to costs associated with the extended fabrication time. Syntheses of binary or ternary oxides using sol-gel precursors are limited by uncontrolled condensation that can lead to "freezing" of a metastable mesostructure possessing little or no structural

Department of Polymer Engineering, University of Akron, Akron, OH 44325.  
Email: vogt@uakron.edu

Electronic Supplementary Information (ESI) available: Chemical structures of MPEGMA, butyl acrylate, CPADB RAFT agent, GPC and <sup>1</sup>H-NMR analysis of PMPEGMA-*b*-PBA block copolymer template, onset temperatures for carbonate and oxide formation based on TGA traces, FTIR spectra for MMCs, AFM images of mesoporous carbonates, high resolution XPS scans for Ni, Co and O peaks, 2-D GISAXS images of MMCs and MMOs, TEM images of mesoporous  $\text{Co}_3\text{O}_4$ , NiO and  $\text{Ni}_x\text{Co}_{(3-x)}\text{O}_4$ , galvanostatic cycling performance of  $\text{Ni}(\text{CO}_3)_y$  and  $\text{Ni}_2\text{Co}(\text{CO}_3)_y$ , charge-discharge profiles for MMOs, Cyclic Voltammetry curves, 4-point probe conductivity of MMOs. See DOI: 10.1039/x0xx00000x

integrity on template removal.<sup>29</sup> In these cases, the final mesostructure is generally very sensitive to a variety of factors: pH of precursor sol, interactions of precursor with template, moisture and processing conditions used. This sensitivity can render the sol-gel strategy tedious for fabricating ordered mesoporous metal oxides.<sup>30, 31</sup>

To overcome these issues and develop a simple and scalable synthesis approach, here we describe a citric acid mediated route for fabrication of ordered mesoporous nickel-cobalt mixed-metal carbonates  $Ni_xCo_{(3-x)}(CO_3)_y$  and mixed-metal oxides  $Ni_xCo_{(3-x)}O_4$ . This method utilizes a complex of metal nitrate and citric acid that has been shown to yield a variety of soft templated mesoporous carbonates and oxides, such as those of cobalt,<sup>32</sup> aluminium,<sup>32</sup> copper,<sup>33</sup> and manganese.<sup>33</sup> We selected this route for the fabrication mesoporous mixed-metal oxides (MMO) due to the lack of an aging requirement, which eliminates a shortcoming of other soft templating methods. Here, we demonstrate this synthesis strategy for the fabrication of ordered mesoporous  $Ni_xCo_{(3-x)}O_4$  through the formation of an intermediate mixed-metal carbonate (MMC)  $Ni_xCo_{(3-x)}(CO_3)_y$ . This intermediate provides an additional opportunity as transition metal carbonates of cobalt<sup>34</sup> and manganese<sup>35</sup> are promising candidates as anodes in lithium ion batteries, but very few reports on use of mixed-metal carbonate (MMC) anodes exist in literature.<sup>36-38</sup> Thus, this methodology should be able to be extended to the synthesis of a wide variety of mesoporous MMCs and MMOs for battery electrodes. We demonstrate that these ordered mesoporous  $Ni_xCo_{(3-x)}O_4$  films act as potentially promising sodium ion battery anodes providing high specific capacity (> 200 mAh/g) at high current densities (> 1 A/g).

## Experimental

### Materials

Cobalt (II) nitrate hexahydrate (reagent grade, 98 %), nickel (II) nitrate hexahydrate (puriss. p.a.,  $\geq 98.5$  %), citric acid (ACS reagent,  $\geq 99.5$  %), ethanol (ACS reagent,  $\geq 99.5$  % 200 proof, absolute), tetrahydrofuran (THF, ACS reagent,  $\geq 99.0$  %, containing 250 ppm BHT as inhibitor), mercaptosuccinic acid (97 %), methoxy poly(ethylene glycol) methacrylate (PMPEGMA, 475 g mol<sup>-1</sup>), butyl acrylate (> 99 %), N, N-Dimethylformamide (DMF) (anhydrous, 99.8 %), and hexane (anhydrous, 95 %) were purchased from Sigma-Aldrich and used as received. 2,2'-Azobis(isobutyronitrile) (AIBN, Sigma-Aldrich, 98 %) was purified by recrystallization from methanol. 4-cyanopentanoic acid dithiobenzoate (CPADB) was synthesized according to prior reports in the literature.<sup>39</sup> Deuterated chloroform (CDCl<sub>3</sub>) (Cambridge Isotope Laboratories, Inc.) was used as received.

For battery testing, sodium perchlorate (NaClO<sub>4</sub>, ACS reagent,  $\geq 98.0\%$ ), ethylene carbonate (EC, anhydrous, 99%) and propylene carbonate (PC, reagent plus, 99.7%) were purchased from Sigma-Aldrich. Sodium metal (99.8% Acros Organics) was used as the reference and counter electrode. For piranha cleaning of the substrates, sulfuric acid (H<sub>2</sub>SO<sub>4</sub>, 95-

98%, J.T. Baker) and hydrogen peroxide (H<sub>2</sub>O<sub>2</sub>, 30%, Fisher Scientific) was used.

### Sample Preparation

Three different substrates were used in these studies: single side polished silicon wafers (Silicon, Inc.), high resistivity (1-10  $\Omega \cdot \text{cm}$ ), 600  $\mu\text{m}$  thick double side polished (DSP) Si wafers for FTIR measurements, and 250  $\mu\text{m}$  thick quartz slides (GM Associates Inc.) sputter coated with gold for electrochemical measurements. The silicon wafers were cleaned with Piranha solution (H<sub>2</sub>SO<sub>4</sub> : H<sub>2</sub>O<sub>2</sub> = 3:1 v/v) at 90 °C for 45 min, followed by multiple rinses with deionized water. These wafers were dried using nitrogen prior to film casting. The gold coated quartz slides were first treated with 10 mM ethanoic mercaptosuccinic acid for 24 h to produce a hydrophilic surface. After 24 h, the quartz substrates were rinsed multiple times with ethanol and dried with nitrogen prior to coating.

To fabricate block copolymer micelle templated thin films, poly[methoxy poly(ethylene glycol) methacrylate]-*block*-poly(butyl acrylate), PMPEGMA-*b*-PBA was used as the structure directing agent. PMPEGMA-*b*-PBA block copolymer template was synthesized by reversible addition-fragmentation chain transfer (RAFT) polymerization<sup>40</sup> following protocol mentioned elsewhere.<sup>41</sup> The number average molecular weight ( $M_n$ ) for PMPEGMA-*b*-PBA is  $5.9 \times 10^4$  g mol<sup>-1</sup> with dispersity ( $D_M$ ) of 1.3. The mole fraction of hydrophilic component ( $f_{PMPEGMA}$ ) in the copolymer is approximately 0.1 as calculated from <sup>1</sup>H-NMR.

Thin films were prepared by first dissolving 188 mg of metal (cobalt and/or nickel) nitrate in 0.6 g ethanol solution. After mixing for 15 min, 62 mg citric acid was added to the nitrate solution and stirred at room temperature for an additional 1 h. In a separate vial, 50 mg of PMPEGMA-*b*-PBA template was dissolved in 1.8 g THF and stirred for 1 h. After mixing for 1 h, the nitrate solution was added dropwise to the block copolymer solution and then stirred for 4-5 h at room temperature prior to film casting. Table 1 lists the solids composition for each of the precursor solutions used to fabricate the films in this work. Films were cast by flow coating<sup>42</sup> at 40 mm/s and a relative humidity of ~ 40-50% RH. The coated films were allowed to dry for 30 min at ambient temperature. The cast films were placed in a preheated muffle furnace (Ney Vulcan 3-130) and heated for 1 h to fabricate the micelle templated carbonates. The calcination conditions are dependent on the composition as shown in Table 1. The calcination temperature for fabricating carbonates was well above the onset temperature of carbonate formation to ensure complete conversion of metal nitrate-citric acid into corresponding metal carbonate. After 1 h, the furnace was passively cooled to room temperature. To generate ordered mesoporous carbonates of  $Ni_2Co(CO_3)_y$  and  $Ni(CO_3)_y$ , micelle templated carbonates of  $Ni_2Co(CO_3)_y$  and  $Ni(CO_3)_y$  obtained previously were calcined in a preheated furnace at 300 °C for additional 20 min and quenched to room temperature. To generate mesoporous metal oxide thin films, a higher temperature was used for calcination of the micelle templated

carbonate films (see Table 1) in a preheated furnace for 30 min. For the oxides, the films were rapidly quenched to room temperature after heating for 30 min. The metal oxide film

thickness was  $110 \pm 15$  nm irrespective of composition to enable direct comparisons.

**Table 1.** Precursor compositions and processing conditions for fabrication of cobalt oxide, nickel oxide and their mixed-metal oxide ( $\text{Ni}_x\text{Co}_{(3-x)}\text{O}_4$ ) composites.

| Sample                                     | $\text{Co}(\text{NO}_3)_2 \cdot 6\text{H}_2\text{O}$<br>(mg) | $\text{Ni}(\text{NO}_3)_2 \cdot 6\text{H}_2\text{O}$<br>(mg) | Citric acid<br>(mg) | PMPEGMA- <i>b</i> -PBA<br>(mg) | Carbonate<br>calcination ( $^\circ\text{C}$ ) | Oxide<br>calcination ( $^\circ\text{C}$ ) |
|--|--|--|---------------------|--------------------------------|---|---|
| $\text{Co}_3\text{O}_4$                    | 188  | -  | 62                  | 50                             | 200   | 300                                       |
| $\text{NiCo}_2\text{O}_4$                  | 143  | 51   | 63                  | 53                             | 220   | 325                                       |
| $\text{Ni}_{1.5}\text{Co}_{1.5}\text{O}_4$ | 94   | 96   | 63                  | 52                             | 240   | 350                                       |
| $\text{Ni}_2\text{CoO}_4$                  | 42   | 148  | 62                  | 55                             | 260   | 365                                       |
| NiO  | -  | 191  | 66                  | 53                             | 265   | 375                                       |

### Characterization

The molecular weight and dispersity of the macro RAFT agent and PMPEGMA-*b*-PBA block copolymer were determined by gel permeation chromatography (GPC). Three water system columns were used for GPC with a HR4, HT2, HR1, HR0.5 styragel, and 500 Å ultrastayragel columns connected in series. GPC analyses in distilled tetrahydrofuran (THF) were performed at 35  $^\circ\text{C}$  using 0.1% (w/v) polymer solutions. Solutions were filtered (0.45  $\mu\text{m}$ ) and 200  $\mu\text{L}$  was injected into the column at an effluent flow rate of 1.0  $\text{mL min}^{-1}$ . The chromatograph was collected using a light scattering detector. The data were interpreted using Omnicsec software v.4.7.0.406. The GPC chromatographs for PMPEGMA and PMPEGMA-*b*-PBA are shown in Supporting Information (Figure S2). The compositions of PMPEGMA and PMPEGMA-*b*-PBA template were determined using  $^1\text{H-NMR}$  (Varian NMRS-500 nuclear magnetic resonance instrument) operating at 500 MHz using deuterated chloroform ( $\text{CDCl}_3$ ) as a solvent (Figures S3 and S4, respectively).

In order to determine the carbonate and oxide formation temperature by thermogravimetric analysis (TGA, TA Instruments, TGA-Q50), crushed powders of the metal nitrate and citric acid were prepared by drying the metal nitrate and citric acid in ethanol / THF mixture without the PMPEGMA-*b*-PBA template at 22  $^\circ\text{C}$  for 8-10 h, followed by heating under vacuum at 50  $^\circ\text{C}$  for another 10 h. TGA was performed using an air purge with 5  $^\circ\text{C}/\text{min}$  ramp rate. The onset of carbonate or oxide formation was determined by the derivative of the mass with respect to temperature, based on three TGA experiments (Figure S5).

Spectroscopic ellipsometry (M-2000, J.A. Woollam) was used to determine the thickness of the metal carbonate and oxide films. The optical properties were modelled with a generalized Kramers-Kronig consistent methodology (GenOsc) in CompleteEASE software (J.A. Woollam) using the wavelength range of 350-1100 nm. The surface morphology of the composite thin films was investigated after each processing step (carbonate and metal oxide) using atomic force microscopy (AFM, Dimension ICON, Veeco). Grazing incidence small angle X-ray scattering (GISAXS) was performed at the X9 beamline of National Synchrotron Light Source (NSLS) at Brookhaven National Laboratory (BNL). An incident X-ray beam of energy of 13.5 keV ( $\lambda = 0.0918$  nm) was used and the

scattering data were collected using a Pilatus detector at a distance of 4.73 m. All samples were measured under vacuum ( $\approx 40$  Pa) at multiple angles, both below and above the critical angle of the sample. Grazing incidence X-ray diffraction (GIXD) was also performed at the X9 beamline of NSLS at BNL to determine the crystal structure of the MMO films. Incident x-ray energy of 13.5 keV was utilized and the scattered intensity was collected on a charged couple device (CCD) WAXS detector. The average crystal size was estimated applying the Scherrer equation<sup>43</sup> to the most intense diffraction peak and assuming  $\beta = 0.9$ .

Fourier Transform Infrared (FTIR) spectra (Thermo Scientific, Nicolet iS50 FT-IR) were obtained in transmission mode through the DSP silicon wafers, collecting 512 scans with a resolution of 8  $\text{cm}^{-1}$  using a Deuterated TriGlycine Sulfate (DTGS) detector. The baseline of the FTIR spectra was corrected using OMNIC software. X-ray photoelectron spectroscopy (XPS, PHI 5000 Versa probe II scanning XPS microprobe, ULVAC-PHI Inc.) with high-resolution scans at energies associated with Ni2p, Co2p and O1s was performed using 0.2 eV step size and pass energy of 23.5 eV. The scans were recorded at a take-off angle of 45 $^\circ$ . Peaks associated with Ni2p, Co2p and O1s were deconvoluted using Multiplex fitting software applying a Shirley baseline correction to quantify the oxidation states of nickel and cobalt in the films.

The electrical conductivity of the mesoporous thin films was determined using four-point probe measurement (Pro-4, Lucas Labs) with a Keithley Series 2400 SourceMeter. The spacing between the pins on the probe head was 1 mm. The electrochemical behavior of the mesoporous films was quantified in a three-electrode system using the mesoporous MMO thin films on gold-coated quartz substrates as the active electrode material and sodium metal as both the counter and reference electrodes. Galvanostatic charge-discharge measurements (CHI660D electrochemical analyzer, CH Instruments) were performed in argon-filled glove box ( $\text{O}_2 < 2.5$  ppm,  $\text{H}_2\text{O} < 0.5$  ppm) using a voltage range of 0.01-3.0 V vs  $\text{Na}/\text{Na}^+$ . 1 M  $\text{NaClO}_4$  in ethylene carbonate: propylene carbonate (EC: PC, 1:1 v/v) served as the electrolyte for the electrochemical measurements. The film anodes were galvanostatically cycled 10 times at current densities varying from 1 A/g to 4 A/g.

## Results and discussion

Metal nitrate-citric acid complexes of nickel and cobalt degrade in a two step process on heating in air; first generating a metal carbonate, which subsequently decomposes into the corresponding metal oxide at higher temperatures.<sup>32</sup> Figure 1 illustrates the compositional dependence on these transformations. Irrespective of composition, two distinct weight-loss steps are visible in all the TGA traces. The first drop corresponds to decomposition of the metal nitrate-citric acid complex to the carbonate. Further heating leads to a near constant mass after formation of the metal carbonate (higher temperatures in the fuchsia region in Figure 1). The onset temperature associated with the carbonate formation is determined from the derivative of this TGA trace. The onset temperature for carbonate formation increases with increasing nickel content in the composite (Figure S5). Cobalt carbonate formation begins around 135 °C while the peak for nickel carbonate occurs at much higher temperature (260 °C). A plateau region following the carbonate onset is observed for these mixed-metal nitrate-citric acid composites instead of two distinct plateaus associated with the pure cobalt and pure nickel carbonate formation. However, the decrease in mass is more gradual for the mixtures, which makes it difficult to assess if only one single phase mixed-metal carbonate (MMC) ( $\text{Ni}_x\text{Co}_{(3-x)}(\text{CO}_3)_y$ ) is formed.

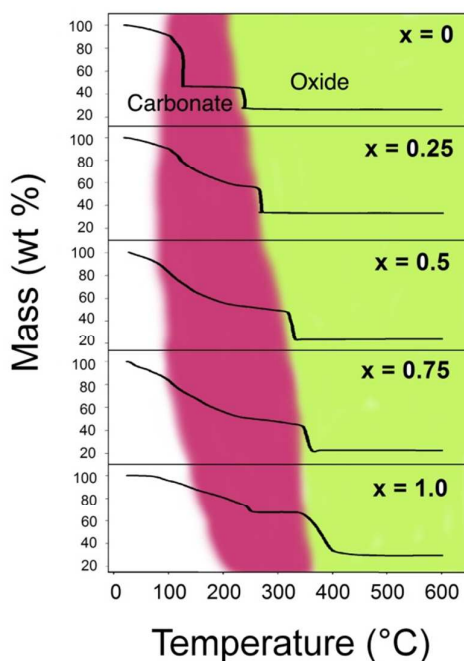


**Fig. 1** TGA traces of metal nitrate-citric acid complex ( $x$  is mole fraction of nickel for the nitrates used) on heating in air. Decomposition of the metal nitrate-citric acid complex occurs in two distinct steps, corresponding to formation of metal carbonate (fuchsia) and decomposition of metal carbonate into corresponding metal oxide (chartreuse). Note that the onset temperature for metal carbonate formation and decomposition into metal oxide shifts towards higher temperature with increasing nickel content in the composite.

At higher temperatures, a second drop in weight is attributed to the decomposition of the metal carbonate into its corresponding metal oxide (chartreuse shading in Figure 1). This decrease is much sharper for the cobalt-nickel mixtures than that associated with the formation of the carbonate. The compositional dependence of the onset temperature of oxide formation is similar to that for the carbonate (Figure S5). For example, the onset temperature for cobalt oxide is approximately 245 °C, but this increases to around 375 °C for nickel oxide. The increase in onset temperature for carbonate or oxide formation with increasing nickel content illustrates that nickel increases the activation energy required for carbonate or oxide formation. The temperature window between the formation of metal carbonate and corresponding metal oxide is around 100 °C. With only two distinct decreases in mass, the TGA analysis suggests that this simple fabrication route can generate single phase  $\text{Ni}_x\text{Co}_{(3-x)}\text{O}_4$  composites.

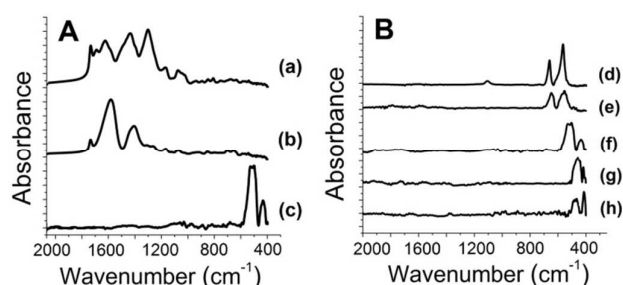


**Fig. 2** (A) FTIR spectra of PMPEGMA-*b*-PBA micelle templated metal nitrate-citric acid film containing with 50 mol% nickel for (a) as cast, (b) carbonate formation at 240 °C for 1 h, and (c) oxide formation at 350 °C for 30 min. (B) FTIR spectra of micelle templated mesoporous (d)  $\text{Co}_3\text{O}_4$ , (e)  $\text{NiCo}_2\text{O}_4$ , (f)  $\text{Ni}_{1.5}\text{Co}_{1.5}\text{O}_4$ , (g)  $\text{Ni}_2\text{CoO}_4$ , and (h) NiO fabricated by first forming the carbonate (heating for 1 h) and subsequently the oxide (heating for 30 min) using the temperatures specified in Table 1.

Insight into the compositional changes during processing is obtained from FTIR. Figure 2A illustrates the FTIR spectra for micelle templated films containing 50:50 (mol:mol) cobalt and nickel nitrate in the precursor through the different stages of the synthesis. The degradation of the template can be confirmed by the loss of the peak at 1740  $\text{cm}^{-1}$ , which corresponds to the C=O vibration from the acrylate. Heating at 240 °C for 1 h leads to significant loss of the template, but does not completely degrade the template. At this temperature, the carbonate is formed as evidenced by the evolution of peaks at 1412  $\text{cm}^{-1}$  and 1587  $\text{cm}^{-1}$  corresponding to C-O bonds. It should be noted that these peak positions are slightly shifted from pure cobalt carbonate.<sup>32</sup> Similar FTIR spectra are observed for the other compositions for the fabrication of the MMCs (Figure S6). After heating this carbonate film at 350 °C for 30 min, the template is now fully decomposed and the peaks associated with the carbonate peaks at 1412  $\text{cm}^{-1}$  and 1587  $\text{cm}^{-1}$  disappear, consistent with decomposition of the carbonate. New peaks centered around 634  $\text{cm}^{-1}$  and 475  $\text{cm}^{-1}$  appear in the spectra corresponding to M-O vibrations from Co-O and Ni-O in  $\text{Ni}_{1.5}\text{Co}_{1.5}\text{O}_4$ .<sup>44</sup> Figure 2B illustrates the change in the FTIR spectra for the MMOs with varying nickel content. Only peaks at low wavenumbers are

observed due to M-O stretching vibrations from tetrahedral and octahedral sites characteristic of cobaltites in the MMO.<sup>32, 45, 46</sup> As the nickel content increases, there is a gradual shift of the peaks associated with the M-O vibrations to lower wavenumbers. These spectra are consistent with a single oxide phase.

To further confirm the formation of single phase MMOs, Figure 3A illustrates the diffraction patterns obtained from GIXD. These profiles exhibit peaks assigned to (111), (220), (311) and (400) planes of the cubic  $\text{Co}_3\text{O}_4$  (PDF card no. 01-078-1969) and MMOs (PDF card no. 01-073-1702), consistent with the formation of  $Fd-3m$  spinel phase.<sup>22, 47, 48</sup> Examination of the (400) peak position (Figure 3B) illustrates that a single peak is present in each case and this peak gradually shifts from  $26.03^\circ$  for  $\text{Co}_3\text{O}_4$  to  $25.04^\circ$  for  $\text{Ni}_2\text{CoO}_4$ . The shift in peak position towards lower  $2\theta$  indicates an increase in lattice spacing between the (400) planes from  $2.04 \text{ \AA}$  ( $\text{NiCo}_2\text{O}_4$ ) to  $2.11 \text{ \AA}$  ( $\text{Ni}_2\text{CoO}_4$ ) with increasing nickel content, which is consistent with prior reports for the spinel phase of these MMOs.<sup>49</sup> Diffraction peaks in NiO can be assigned to (111) and (200) planes of the  $Fm-3m$  cubic crystal structure (PDF card no. 00-004-0835). X-ray photoelectron spectroscopy indicates nickel to be present as primarily  $\text{Ni}^{2+}$  with some  $\text{Ni}^{3+}$  in the oxide. Thus, the pure nickel oxide formed through the nickel nitrate-citric acid route predominantly forms NiO with a small fraction of  $\text{Ni}_2\text{O}_3$  as well on the surface of the thin films. Applying the Scherrer equation<sup>43</sup> to the most intense peak from GIXD data of MMOs, the average crystallite size decreases from  $4.2 \text{ nm}$  for  $\text{Co}_3\text{O}_4$  to  $2.3 \text{ nm}$  for NiO. The average crystallite size formed in mesoporous  $\text{NiCo}_2\text{O}_4$  thin film is  $3.6 \text{ nm}$  while in case of  $\text{Ni}_2\text{CoO}_4$ , much smaller crystals of average size  $2.3 \text{ nm}$  are formed. This indicates that the crystallization behavior of the MMOs is impacted by the chemical composition of the composite and the processing conditions utilized.

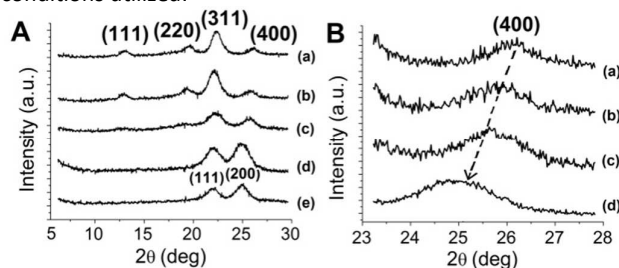


**Fig. 3** (A) 1-D GIXD profiles for (a)  $\text{Co}_3\text{O}_4$ , (b)  $\text{NiCo}_2\text{O}_4$ , (c)  $\text{Ni}_{1.5}\text{Co}_{1.5}\text{O}_4$ , (d)  $\text{Ni}_2\text{CoO}_4$ , and (e) NiO. (B) Diffraction profiles from the (400) plane for (a)  $\text{Co}_3\text{O}_4$ , (b)  $\text{NiCo}_2\text{O}_4$ , (c)  $\text{Ni}_{1.5}\text{Co}_{1.5}\text{O}_4$  and (d)  $\text{Ni}_2\text{CoO}_4$ . There is a shift in the (400) peak position to lower  $2\theta$  with increasing nickel content.

X-ray photoelectron spectroscopy analysis (Figure S8) also corroborates formation of single phase  $\text{Ni}_x\text{Co}_{(3-x)}\text{O}_4$ , wherein the defect oxygen concentration is found to increase in the MMO composite with increasing nickel content due to intercalation of nickel within the cobalt crystal lattice.<sup>49</sup> Moreover, the chemical composition of MMOs determined from XPS survey scans is found to be close to the theoretical values from the initial precursor solutions (Table 2).

**Table 2.** Atomic ratios in MMO films determined from XPS survey scans

| Sample                                     | Atomic ratio<br>(Ni:Co:O) |
|--|---------------------------|
| $\text{NiCo}_2\text{O}_4$                  | (1 : 2.18 : 4)            |
| $\text{Ni}_{1.5}\text{Co}_{1.5}\text{O}_4$ | (1.72 : 1.53 : 4)         |
| $\text{Ni}_2\text{CoO}_4$                  | (2.28 : 0.84 : 4)         |

The surface morphology of these films is characterized by Atomic Force Microscopy (AFM). Figure 4 illustrates the surface morphology of the micelle templated films after carbonate formation. All materials exhibit clear evidence of templating by spherical PMPEGMA-*b*-PBA micelles. A common length-scale associated with the center-to-center packing of the micelles is observed:  $33.2 \text{ nm}$  for  $\text{Co}(\text{CO}_3)_y$  and  $31.3 \text{ nm}$  for  $\text{Ni}(\text{CO}_3)_y$ . In case of the MMCs, this distance does not systematically vary with nickel content ( $32.7 \text{ nm}$  for  $\text{NiCo}_2(\text{CO}_3)_y$ ,  $31.2 \text{ nm}$  for  $\text{Ni}_{1.5}\text{Co}_{1.5}(\text{CO}_3)_y$  and  $32.3 \text{ nm}$  for  $\text{Ni}_2\text{Co}(\text{CO}_3)_y$ ). The relative invariance of the structure with composition suggests that the micelle self-assembly process is not significantly impacted by precursor selection. Note that these films still contain some of the block copolymer template (Figure S6).

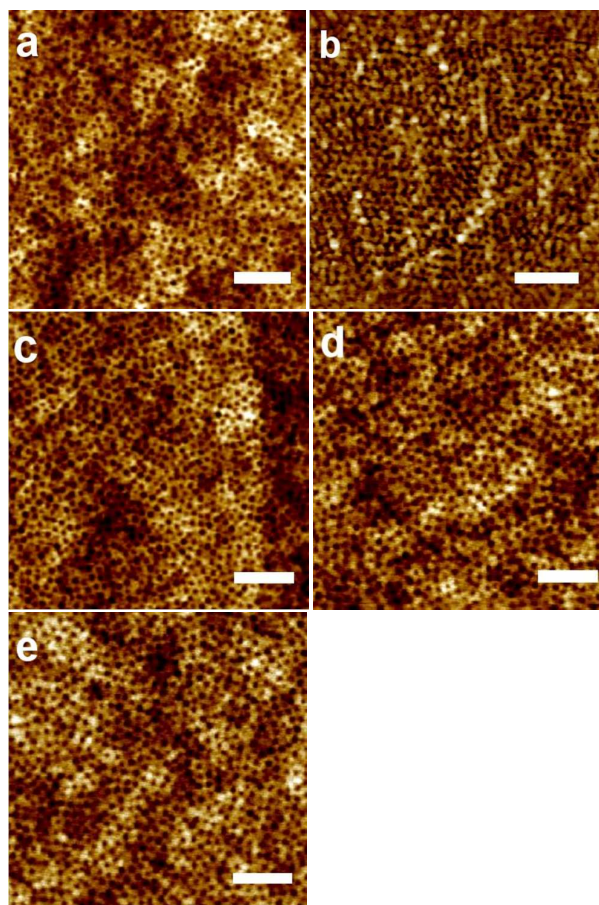


**Fig. 4** AFM micrographs of micelle templated (a)  $\text{Co}(\text{CO}_3)_y$ , (b)  $\text{NiCo}_2(\text{CO}_3)_y$ , (c)  $\text{Ni}_{1.5}\text{Co}_{1.5}(\text{CO}_3)_y$ , (d)  $\text{Ni}_2\text{Co}(\text{CO}_3)_y$ , and (e)  $\text{Ni}(\text{CO}_3)_y$ . A microphase separated morphology is present in all cases. (Scale bar =  $200 \text{ nm}$  in all micrographs)

To obtain template-free mesoporous  $\text{Ni}_2\text{Co}(\text{CO}_3)_y$  and  $\text{Ni}(\text{CO}_3)_y$  films, the micelle templated carbonates (shown in Figure 4) were heated for additional 20 min at 300 °C. The removal of PMPEGMA-*b*-PBA template was confirmed by FTIR spectroscopy (Figure S7). The templated structure is maintained in the carbonates even after complete removal of block copolymer template (Figure S7). Mesoporous  $\text{Co}(\text{CO}_3)_y$ ,  $\text{NiCo}_2(\text{CO}_3)_y$  and  $\text{Ni}_{1.5}\text{Co}_{1.5}(\text{CO}_3)_y$  could not be fabricated due to decomposition of carbonate to its corresponding oxide prior to complete removal of the block copolymer template.

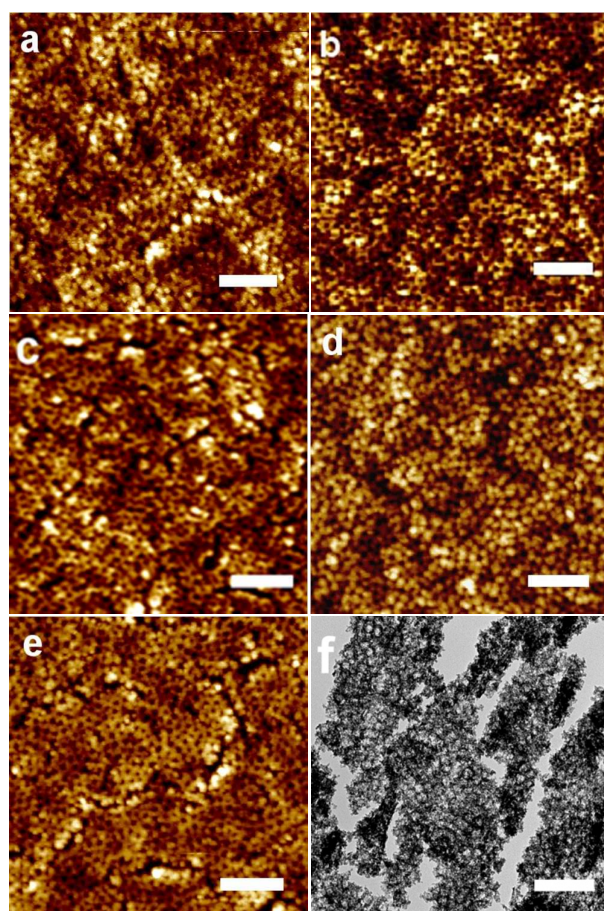


**Fig. 5** AFM micrographs of templated mesoporous (a)  $\text{Co}_3\text{O}_4$ , (b)  $\text{NiCo}_2\text{O}_4$ , (c)  $\text{Ni}_{1.5}\text{Co}_{1.5}\text{O}_4$ , (d)  $\text{Ni}_2\text{CoO}_4$ , and (e)  $\text{NiO}$ . The templated porous structure is maintained after decomposition of metal carbonate and complete removal of block copolymer template. (f) TEM micrograph of  $\text{Ni}_{1.5}\text{Co}_{1.5}\text{O}_4$  film that has been scrapped from the substrate (Scale bar = 200 nm)

Figure 5 illustrates the surface morphology of the mesoporous oxides. The carbonate decomposition appears to degrade the packing of the micelles and lead to some small cracks. The extent of cracking increases for the higher nickel content films (which are subjected to higher calcination temperatures). Although these higher temperatures will lead to larger stresses due to mismatch in the coefficient of thermal expansion between the mesoporous material and the silicon substrate, we attribute the cracks primarily to the confined inorganic framework shrinkage in these supported films. This leads to anisotropic shrinkage<sup>50, 51</sup> and potential loss of the

ordered nanostructure.<sup>52</sup> This shrinkage leads to a decrease in common length scale associated with micelle packing from 33.2 nm for cobalt carbonate to 28.6 nm for cobalt oxide, while the center-to-center distance between pores decreases from 31.3 nm for nickel carbonate to 29.6 nm for nickel oxide. Similar decrease in length scale is also observed on conversion of the MMCs to corresponding MMOs. The templated mesopores formed in all the MMO thin films are  $15 \pm 3$  nm wide based on AFM micrographs. These pore diameters agree with the pore size ( $14 \pm 4$  nm) observed in the TEM micrograph (Figure 5f). Despite the large stresses applied during template removal and conversion to oxide, the templated porous structure is maintained in all the films (Figure 5) based on surface topography.

However, these AFM micrographs only provide information about the surface of these templated films. GISAXS interrogates the structure through the thickness over a large area. Figure 6A illustrates the 1-D in-plane GISAXS profiles obtained for the templated MMCs films; a broad primary peak and a weak secondary peak are present. Based on the primary peak position, the *d*-spacing is nearly invariant of composition decreasing from 33.9 nm for  $\text{Co}(\text{CO}_3)_y$  to 31.7 nm for  $\text{Ni}(\text{CO}_3)_y$ , consistent with the spacing determined from AFM (33.2 nm and 31.3 nm, respectively). The secondary peak in the GISAXS profiles illustrates the long-range order in these MMC thin films. However, with increasing nickel content, this second order peak becomes broader indicating some loss of in-plane correlations. The ellipsoidal SAXS pattern of MMCs (Figure S10) indicates presence of distorted body-centered cubic (bcc) mesostructure in the MMC thin films, with film shrinkage primarily occurring in the out-of-plane direction (normal to the substrate) during the carbonate heating stage.<sup>53, 54</sup> The primary and secondary peaks can be indexed to (110) and (220) bcc planes, respectively.

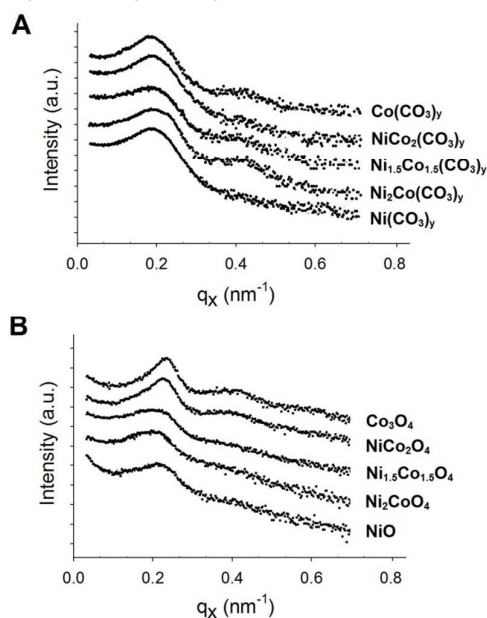


**Fig. 6** 1-D plots extracted from GISAXS data for (A) mixed metal carbonates ( $\text{Ni}_x\text{Co}_{3-x}(\text{CO}_3)_y$ ) and (B) mesoporous mixed metal oxides ( $\text{Ni}_x\text{Co}_{3-x}\text{O}_4$ ) at 0.2° incident angle.

Figure 6B illustrates the GISAXS profiles for the mesoporous MMOs. A distinct primary peak corresponding to (110) plane is observed in all cases, which indicates that the cubic mesostructure is maintained through template removal and oxide formation. However, the primary peak position shifts to a higher  $q_x$ , compared to the corresponding metal carbonates. In case of pure cobalt oxide, the  $d$ -spacing decreases from 33.9 nm for the carbonate to 28.9 nm for the oxide; a 14.6% decrease in the in-plane correlations. A similar decrease (13.8%) in  $d$ -spacing due to shrinkage of inorganic framework was also observed in AFM. Interestingly, the largest  $d$ -spacing for the oxides is found for  $\text{Ni}_{1.5}\text{Co}_{1.5}\text{O}_4$  (30.9 nm), which corresponds to 8.6% contraction from the carbonate to the oxide. This indicates that the structure of templated films evolves during decomposition of carbonate into corresponding mesoporous metal oxide. Similar to MMCS, a weak second order peak is also visible in the scattering profiles for these mesoporous MMO films. To confirm the porous structure of the mixed-metal oxides, thin films were scrapped from silicon wafers and powdered samples were prepared for TEM imaging (Figure S12). All the images illustrate well-ordered and templated porous architectures for these oxides. The average pore diameter obtained in these mesoporous oxides is  $14 \pm 4$  nm, which matches well with the pore width determined from AFM micrographs (Figure 5). Also the inorganic walls are comprised of individual nanoparticles that are  $4.5 \pm 1.5$  nm in diameter, which is similar to the size scale suggested by the GIXD analysis.

Block copolymer templated mesoporous metal oxides are known to enhance the performance of battery anode materials as compared their non-porous analogs due to facile electrolyte diffusion and high surface area.<sup>11, 13</sup> The well-defined nanoporous architecture of these MMO thin films should allow for efficient charge storage at high current densities.<sup>13, 55, 56</sup> This metal nitrate-citric acid route can fabricate ordered mesoporous metal oxide with porosities as high as 40%.<sup>41</sup> To test the impact of this porosity and interconnected porous architecture on the charge storage capabilities in sodium ion battery, ordered mesoporous  $\text{Co}_3\text{O}_4$  and NiO thin film anodes were galvanostatically cycled at a high current density of 1A/g (Figure 7). The current densities utilized here are much higher than those reported in previous studies for use of  $\text{Co}_3\text{O}_4$ , NiO or  $\text{NiCo}_2\text{O}_4$  anodes in sodium ion battery.<sup>19, 21, 57</sup> In this case, the thin film geometry provides a facile route to screen the MMO compositions to avoid convolution with the effect associated with binder chemistry, carbon black and slurry preparation.

Mesoporous cobalt oxide and nickel oxide thin film anodes provide a high initial discharge capacity of 602 mAh/g and 619 mAh/g, respectively. Based on the oxide film thickness (~110 nm) and anode dimensions, the volumetric capacity of these active materials in the first discharge cycle is found to be 2488 mAh/cm<sup>3</sup> ( $\text{Co}_3\text{O}_4$ ) and 2572 mAh/cm<sup>3</sup> (NiO) (Figure S17). These initial discharge capacity values are higher than those previously reported, despite the higher current density employed here.<sup>19, 57</sup> High current densities lead to electrolyte ion mass transfer issues and generally low capacity. We

attribute the higher specific capacity<sup>58, 59</sup> of these mesoporous cobalt oxide and nickel oxide at high current densities to the interconnected porous structure, short paths within the metal oxide and the continuous nature of the film. The interconnected porous electrode architecture helps to alleviate mass transfer issues and the nano-dimension of the inorganic walls provides shorter diffusion paths for sodium ions, which should lead to enhancement in performance of metal oxide anode.<sup>55, 60</sup>

These metal oxide anodes, however, suffer significant capacity fade providing a low specific capacity of 59 mAh/g (242 mAh/cm<sup>3</sup>) in case of  $\text{Co}_3\text{O}_4$  and 132 mAh/g (483 mAh/cm<sup>3</sup>) in case of NiO after 10 cycles. Ideally, anode materials are galvanostatically cycled at low current densities to form a stable solid electrolyte interface (SEI) layer on the electrode, followed by charging-discharging at high current densities in subsequent cycles. However, the high current density (1 A/g) used in our system likely hinders the formation of a stable solid electrolyte interface, which may contribute partially to the large capacity fade in these mesoporous anodes. The initial drop in specific capacity can also be attributed to side reactions occurring with the electrolyte and irreversible conversion reactions taking place in the first few cycles.<sup>66</sup> Cyclic voltammetry of the mesoporous thin films (Figure S14) at a scan rate of 2 mV/s provides further insight into the conversion reactions and capacity fade taking place in  $\text{Co}_3\text{O}_4$  and NiO anodes. The mesoporous  $\text{Co}_3\text{O}_4$  anode exhibits an intense cathodic peak at 0.46 V corresponding to partial reduction of  $\text{Co}^{3+}$  and  $\text{Co}^{2+}$  to metallic Co. The broad peak centered around 0.8 V corresponds to  $\text{Na}_2\text{O}$  formation accompanied by electrolyte decomposition.<sup>19</sup> The anodic peak corresponding to Co oxidation occurs at approximately 1.5 V. As illustrated in Figure S14, the area under the CV curves progressively decreases upon successive cycling, consistent with the poor cycling stability of  $\text{Co}_3\text{O}_4$  anode (Figure 7A) at high rates.

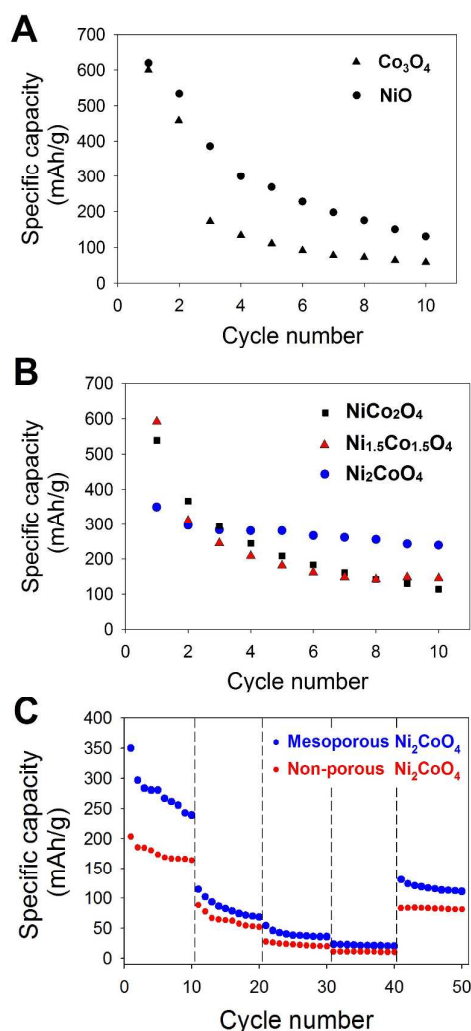
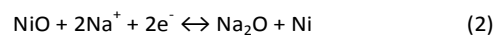


**Fig. 7** (A) Cycling stability of mesoporous cobalt oxide (▲) and nickel oxide (●) film anodes for sodium ion batteries at a current density of 1 A/g, (B) Comparison of the MMOs as anodes subjected to galvanostatic cycling over 10 cycles with a potential window of 0.01–3.0 V at current density of 1 A/g: NiCo<sub>2</sub>O<sub>4</sub> (■), Ni<sub>1.5</sub>Co<sub>1.5</sub>O<sub>4</sub> (▲), and Ni<sub>2</sub>CoO<sub>4</sub> (●). (C) Specific discharge capacities of Ni<sub>2</sub>CoO<sub>4</sub> anode subjected to galvanostatic cycling at varying current densities

In the case of the mesoporous NiO anode (Figure S14B), the cyclic voltammogram exhibits a broad peak centred around 1.0 V corresponding to the reduction of NiO to metallic Ni, while the broad cathodic peak in voltage range of 0.1–0.3 V corresponds to SEI formation and conversion reactions.<sup>65</sup> The anodic peak corresponding to Ni oxidation is observed around 1.2 V and 1.7 V in the anodic curve. The low intensity of cathodic peak in the subsequent cycles indicates irreversible conversion reactions taking place in the NiO anode at high rates, leading to poor cycling stability of the mesoporous electrode.

Theoretically, the reversible conversion reactions during sodium insertion-deinsertion in the metal oxides can be described as:



On galvanostatically cycling of the mesoporous MMO anodes of NiCo<sub>2</sub>O<sub>4</sub> and Ni<sub>1.5</sub>Co<sub>1.5</sub>O<sub>4</sub> a high initial capacity of 538 mAh/g and 591 mAh/g is obtained but these anodes exhibit poor capacity retention (only 21% and 25%) at the end of 10 cycles. The equivalent volumetric capacity for the first discharge cycle is 2275 mAh/cm<sup>3</sup> in case of NiCo<sub>2</sub>O<sub>4</sub> and 2671 mAh/cm<sup>3</sup> for Ni<sub>1.5</sub>Co<sub>1.5</sub>O<sub>4</sub>. Doping of cobalt oxide films with nickel ideally leads to significantly enhanced electronic conductivity of Ni<sub>x</sub>Co<sub>(3-x)</sub>O<sub>4</sub>.<sup>61, 62</sup> Similar enhancement in electronic conductivity is observed in our case as the conductivity increases from  $0.06 \pm 0.02 \text{ S cm}^{-1}$  for NiCo<sub>2</sub>O<sub>4</sub> to  $0.23 \pm 0.06 \text{ S cm}^{-1}$  for Ni<sub>2</sub>CoO<sub>4</sub> (Figure S19). Such increase in electronic conductivity is typically associated with increase in doping of Ni<sup>3+</sup> within the octahedral sites of Ni<sub>x</sub>Co<sub>(3-x)</sub>O<sub>4</sub>. This agrees with the XPS measurements (Figure S8), which illustrated an increase in Ni<sup>3+</sup> concentration within the crystal lattice upon increasing the nickel component in the MMO. The enhancement in electronic conductivity should provide faster electron transport in the mesoporous Ni<sub>x</sub>Co<sub>(3-x)</sub>O<sub>4</sub> anodes, but this still does not lead to improved high rate performance. Nonetheless, the crystal structure remains after cycling as shown in Figure S18. Cyclic voltammetry curves (Figure S15) further indicate poor cycling capabilities of these MMO anodes at high rates, as evidenced by decrease in redox peak intensities with successive cycling.

The mesoporous Ni<sub>2</sub>CoO<sub>4</sub> anode, on the other hand, provides a lower initial discharge capacity 352 mAh/g (1711 mAh/cm<sup>3</sup>) but maintains 68% of its initial capacity at the end of 10 cycles. This represents a significant improvement on the capacity retention of previously reported NiCo<sub>2</sub>O<sub>4</sub> anode, which exhibited only 32% capacity retention after 2 cycles.<sup>21</sup> Cyclic voltammetry curve of Ni<sub>2</sub>CoO<sub>4</sub> thin film anode further (Figure S15) illustrates enhanced cycling capabilities of this MMO composition, where the CV curves almost overlap each other after 10 cycles. Even on galvanostatically cycling Ni<sub>2</sub>CoO<sub>4</sub> anode at significantly high current density of 2 A/g, a discharge capacity of 118 mAh/g (560 mAh/cm<sup>3</sup>) is obtained while at 4 A/g current density. This value decreases to 24 mAh/g (114 mAh/cm<sup>3</sup>) with 88% capacity retention after 10 cycles on cycling at 4 A/g. In comparison, a non-templated, non-porous Ni<sub>2</sub>CoO<sub>4</sub> thin film anode offers a much lower initial discharge capacity of 203 mAh/g at 1 A/g suffering capacity fade upon successive cycling (Figure 7). This discharge capacity is only 58% as compared to the templated mesoporous Ni<sub>2</sub>CoO<sub>4</sub> anode. At higher discharge rates of 2 A/g, a lower capacity of 88 mAh/g is obtained and this value drops to 68 mAh/g after 10 additional cycles. Even after galvanostatically cycling at higher rates of 3 A/g and 4 A/g, the templated mesoporous Ni<sub>2</sub>CoO<sub>4</sub> thin film anode offers higher capacity illustrating the ease of electrolyte diffusion in porous media at high rates and higher electro-active surface area afforded by the mesoporous anode. On reducing the current density back to 1 A/g, a reversible capacity of 131 mAh/g (639 mAh/cm<sup>3</sup>) is obtained in

case of the templated mesoporous Ni<sub>2</sub>CoO<sub>4</sub> anode, while only 83 mAh/g capacity is obtained from the non-porous film. The templated mesoporous Ni<sub>2</sub>CoO<sub>4</sub> thin film anode architecture allows for strain accommodation during Na<sup>+</sup> ion insertion and improved transport through the material in comparison to the non-porous, dense Ni<sub>2</sub>CoO<sub>4</sub> anode.

The comparatively poor cycling stability of MMO anodes with lower nickel content might be due to the formation of surface-active carbonate ions on exposure of MMO anodes to ambient atmosphere, prior to the transfer to the glove-box for testing.<sup>63</sup> Similar carbonate formation has been reported in case of sodium layered transition metal oxide cathodes leading to much lower discharge capacity as compared to air-protected electrodes. However, with higher nickel content in the MMO (Ni<sub>2</sub>CoO<sub>4</sub>), enhanced stability towards carbonate formation<sup>63</sup> leads to significantly better cycling stability and charge storage performance,<sup>64</sup> as in observed in case of Ni<sub>2</sub>CoO<sub>4</sub> anodes. Similarly, the larger lattice spacing between the crystal planes in Ni<sub>2</sub>CoO<sub>4</sub> and enhanced electronic conductivity compared to other MMOs can assist with the reversible insertion-deinsertion of sodium ions at high current densities, enhancing the cycling stability in the process. Although the specific capacities and reversible cycling capabilities of MMO anodes obtained here are not the highest reported for metal oxide based sodium battery anodes, these materials are not optimized into composites (carbon black + binder) associated with anodes for coin cells. The performance of these materials nonetheless are comparable or slightly higher than those obtained for TiO<sub>2</sub> based anodes<sup>18,66,67</sup> (one of the most studied anode material). The primary aim of this study was to develop simple fabrication strategies that allow for initial screening of MMO compositions and their electrochemical behavior, for potential use as sodium ion battery anodes. Further optimization of electrolytes accompanied by addition of carbon black and binder likely will lead to improved overall battery performance.

The metal nitrate-citric acid route offers a simple strategy to fabricate mixed-metal oxide anodes that are templated by block copolymers. This generalized fabrication method should be readily extendable to various complex metal oxides for high performance sodium ion battery anodes as well as hosts of other applications.

## Conclusions

In this work, we have extended a simple strategy based on metal nitrate-citric acid complex as a precursor in order to fabricate block copolymer micelle-templated mesoporous mixed-metal carbonates (MMCs) and mixed-metal oxides (MMOs) of nickel and cobalt. With no aging requirements, this method provides scalable generalized route to fabricate variety of mesoporous carbonates and/or oxides of mixed transition metals. The mesoporous nickel-cobalt MMO thin films are found to maintain an ordered porous structure through the film thickness direction with pore width around 14 nm. This porous structure provides high surface area and interconnecting pathways for electrolyte diffusion, due to

which the MMOs act as efficient high-rate sodium ion battery anodes. These mesoporous Ni<sub>x</sub>Co<sub>(3-x)</sub>O<sub>4</sub> thin film anodes are found to provide superior charge storage and enhanced cycling stability as compared to their bulk analogs. Mesoporous Ni<sub>2</sub>CoO<sub>4</sub> provides initial discharge capacity of 352 mAh/g with good capacity retention when galvanostatically cycled at constant current density of 1 A/g.

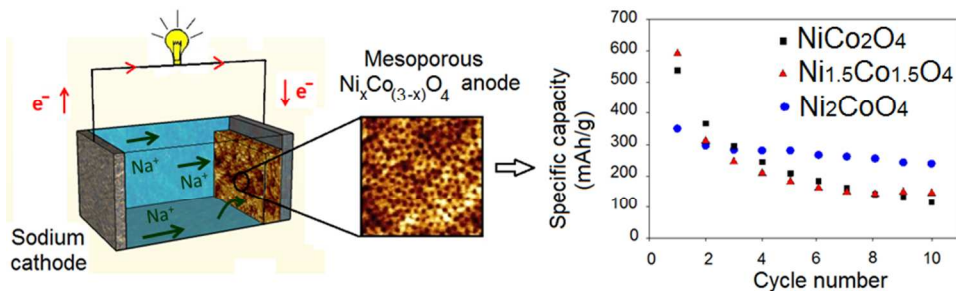
## Acknowledgements

This work has been partially supported by the National Science Foundation under grant CBET-1336057. Research was carried out in part at the Center for Functional Nanomaterials, Brookhaven National Laboratory, which is supported by the U.S. Department of Energy, Office of Basic Energy Sciences, under Contract No. DE-AC02-98CH10886. The authors thank Kevin Yager (BNL), Byeongdu Lee (APS), Yuanzhong Zhang and Zhe Qiang for their assistance with the GISAXS/GIXD measurements and their interpretation. The authors also thank Dr. Zhorro Nikolov for his assistance with XPS data analysis. Yu-Ming Chen, Kewei Liu and Dr. Yu Zhu are acknowledged for their help with battery testing measurements.

## References

1. T. Brezesinski, C. Erpen, K. Iimura and B. Smarsly, *Chem. Mater.*, 2005, **17**, 1683-1690.
2. P. D. Yang, D. Y. Zhao, D. I. Margolese, B. F. Chmelka and G. D. Stucky, *Chem. Mater.*, 1999, **11**, 2813-2826.
3. Y. Wan, Y. F. Shi and D. Y. Zhao, *Chem. Commun.*, 2007, 897-926.
4. Y. H. Deng, J. Wei, Z. K. Sun and D. Y. Zhao, *Chem. Soc. Rev.*, 2013, **42**, 4054-4070.
5. I. E. Rauda, V. Augustyn, B. Dunn and S. H. Tolbert, *Acc. Chem. Res.*, 2013, **46**, 1113-1124.
6. C. Jo, J. Hwang, H. Song, A. H. Dao, Y. T. Kim, S. H. Lee, S. W. Hong, S. Yoon and J. Lee, *Adv. Funct. Mater.*, 2013, **23**, 3747-3754.
7. J. Wei, D. D. Zhou, Z. K. Sun, Y. H. Deng, Y. Y. Xia and D. Y. Zhao, *Adv. Funct. Mater.*, 2013, **23**, 2322-2328.
8. A. Taguchi and F. Schuth, *Microporous Mesoporous Mater.*, 2005, **77**, 1-45.
9. K. Nakajima, T. Fukui, H. Kato, M. Kitano, J. N. Kondo, S. Hayashi and M. Hara, *Chem. Mater.*, 2010, **22**, 3332-3339.
10. S. B. Wang, *Microporous Mesoporous Mater.*, 2009, **117**, 1-9.
11. F. Jiao, J. L. Bao, A. H. Hill and P. G. Bruce, *Angew. Chem., Int. Ed.*, 2008, **47**, 9711-9716.
12. Z. Z. Lin, W. B. Yue, D. Z. Huang, J. Y. Hu, X. Y. Zhang, Z. Y. Yuan and X. J. Yang, *RSC Adv.*, 2012, **2**, 1794-1797.
13. J. Haetge, P. Hartmann, K. Brezesinski, J. Janek and T. Brezesinski, *Chem. Mater.*, 2011, **23**, 4384-4393.
14. K. Brezesinski, J. Haetge, J. Wang, S. Mascotto, C. Reitz, A. Rein, S. H. Tolbert, J. Perlich, B. Dunn and T. Brezesinski, *Small*, 2011, **7**, 407-414.
15. V. Augustyn, J. Come, M. A. Lowe, J. W. Kim, P. L. Taberna, S. H. Tolbert, H. D. Abruna, P. Simon and B. Dunn, *Nat. Mater.*, 2013, **12**, 518-522.
16. V. Palomares, P. Serras, I. Villaluenga, K. B. Hueso, J. Carretero-Gonzalez and T. Rojo, *Energy Environ. Sci.*, 2012, **5**, 5884-5901.
17. M. D. Slater, D. Kim, E. Lee and C. S. Johnson, *Adv. Funct. Mater.*, 2013, **23**, 947-958.

18. L. M. Wu, D. Buchholz, D. Bresser, L. G. Chagas and S. Passerini, *J. Power Sources*, 2014, **251**, 379-385.
19. M. M. Rahman, A. M. Glushenkov, T. Ramireddy and Y. Chen, *Chem. Commun.*, 2014, **50**, 5057-5060.
20. B. Koo, S. Chattopadhyay, T. Shibata, V. B. Prakapenka, C. S. Johnson, T. Rajh and E. V. Shevchenko, *Chem. Mater.*, 2013, **25**, 245-252.
21. R. Alcantara, M. Jaraba, P. Lavela and J. L. Tirado, *Chem. Mater.*, 2002, **14**, 2847-2848.
22. Q. F. Wang, B. Liu, X. F. Wang, S. H. Ran, L. M. Wang, D. Chen and G. Z. Shen, *J. Mater. Chem.*, 2012, **22**, 21647-21653.
23. R. Ding, L. Qi, M. J. Jia and H. Y. Wang, *J. Appl. Electrochem.*, 2013, **43**, 903-910.
24. G. Gao, H. B. Wu, S. Ding, L.-M. Liu and X. W. D. Lou, *Small*, 2015, **11**, 804-808.
25. H. C. Chien, W. Y. Cheng, Y. H. Wang and S. Y. Lu, *Adv. Funct. Mater.*, 2012, **22**, 5038-5043.
26. C. Z. Yuan, H. B. Wu, Y. Xie and X. W. Lou, *Angew. Chem., Int. Ed.*, 2014, **53**, 1488-1504.
27. Y. Li, L. L. Zou, J. Li, K. Guo, X. W. Dong, X. W. Li, X. Z. Xue, H. F. Zhang and H. Yang, *Electrochim. Acta*, 2014, **129**, 14-20.
28. V. Luca, G. J. A. A. Soler-Illia, P. C. Angelome, P. Y. Steinberg, E. Drabarek and T. L. Hanley, *Microporous Mesoporous Mater.*, 2009, **118**, 443-452.
29. G. J. D. Soler-illia, C. Sanchez, B. Lebeau and J. Patarin, *Chem. Rev.*, 2002, **102**, 4093-4138.
30. G. Soler-Illia and C. Sanchez, *New J. Chem.*, 2000, **24**, 493-499.
31. G. Soler-Illia, E. Socolan, A. Louis, P. A. Albouy and C. Sanchez, *New J. Chem.*, 2001, **25**, 156-165.
32. B. Eckhardt, E. Ortel, D. Bernsmeier, J. Polte, P. Strasser, U. Vainio, F. Emmerling and R. Kraehnert, *Chem. Mater.*, 2013, **25**, 2749-2758.
33. Y. Zhang, S. M. Bhaway, Y. Wang, K. A. Cavicchi, M. L. Becker and B. D. Vogt, *Chem. Commun.*, 2015, **51**, 4997-5000.
34. L. W. Su, Z. Zhou, X. Qin, Q. W. Tang, D. H. Wu and P. W. Shen, *Nano Energy*, 2013, **2**, 276-282.
35. M. J. Aragon, B. Leon, C. P. Vicente and J. L. Tirado, *J. Power Sources*, 2011, **196**, 2863-2866.
36. Y. Sharma, N. Sharma, G. V. S. Rao and B. V. R. Chowdari, *J. Mater. Chem.*, 2009, **19**, 5047-5054.
37. S. Mirhashemihaghghi, B. Leon, C. P. Vicente, J. L. Tirado, R. Stoyanova, M. Yoncheva, E. Zhecheva, R. S. Puche, E. M. Arroyo and J. R. de Paz, *Inorg. Chem.*, 2012, **51**, 5554-5560.
38. J. Q. Zhao and Y. Wang, *J. Mater. Chem. A*, 2014, **2**, 14947-14956.
39. S. H. Thang, Y. K. Chong, R. T. A. Mayadunne, G. Moad and E. Rizzardo, *Tetrahedron Lett.*, 1999, **40**, 2435-2438.
40. Y. K. Chong, T. P. T. Le, G. Moad, E. Rizzardo and S. H. Thang, *Macromolecules*, 1999, **32**, 2071-2074.
41. M. C. Burroughs, S. M. Bhaway, P. Tangvijitsakul, K. A. Cavicchi, M. D. Soucek, B. D. Vogt, *J. Phys. Chem. C*, 2015, **119**, 12138-12148.
42. C. M. Stafford, K. E. Roskov, T. H. Epps and M. J. Fasolka, *Rev. Sci. Instrum.*, 2006, **77**, 7.
43. U. Holzwarth and N. Gibson, *Nat. Nanotechnol.*, 2011, **6**, 534-534.
44. G. Y. He, L. Wang, H. Q. Chen, X. Q. Sun and X. Wang, *Mater. Lett.*, 2013, **98**, 164-167.
45. B. Pejova, T. Kocareva, M. Najdoski and I. Grozdanov, *Appl. Surf. Sci.*, 2000, **165**, 271-278.
46. L. L. Li, S. J. Peng, Y. L. Cheah, P. F. Teh, J. Wang, G. Wee, Y. W. Ko, C. L. Wong and M. Srinivasan, *Chem. - Eur. J.*, 2013, **19**, 5892-5898.
47. R. B. Rakhi, W. Chen, D. Y. Cha and H. N. Alshareef, *Nano Lett.*, 2012, **12**, 2559-2567.
48. H. Liu, G. X. Wang, J. Liu, S. Z. Qiao and H. J. Ahn, *J. Mater. Chem.*, 2011, **21**, 3046-3052.
49. Z. Ren, V. Botu, S. B. Wang, Y. T. Meng, W. Q. Song, Y. B. Guo, R. Ramprasad, S. L. Suib and P. X. Gao, *Angew. Chem., Int. Ed.*, 2014, **53**, 7223-7227.
50. D. Grosso, A. R. Balkenende, P. A. Albouy, A. Ayril, H. Amenitsch and F. Babonneau, *Chem. Mater.*, 2001, **13**, 1848-1856.
51. S. Tanaka, Y. Katayama, M. P. Tate, H. W. Hillhouse and Y. Miyake, *J. Mater. Chem.*, 2007, **17**, 3639-3645.
52. L. Song, D. Feng, N. J. Fredin, K. G. Yager, R. L. Jones, Q. Wu, D. Zhao and B. D. Vogt, *ACS Nano*, 2010, **4**, 189-198.
53. W. Ruland and B. M. Smarsly, *J. Appl. Crystallogr.*, 2007, **40**, 409-417.
54. E. Ortel, A. Fischer, L. Chuenchom, J. Polte, F. Emmerling, B. Smarsly and R. Kraehnert, *Small*, 2012, **8**, 298-309.
55. E. Kang, Y. S. Jung, G. H. Kim, J. Chun, U. Wiesner, A. C. Dillon, J. K. Kim and J. Lee, *Adv. Funct. Mater.*, 2011, **21**, 4349-4357.
56. J. Haetge, I. Djerdj and T. Brezesinski, *Chem. Commun.*, 2012, **48**, 6726-6728.
57. Y. Z. Jiang, M. J. Hu, D. Zhang, T. Z. Yuan, W. P. Sun, B. Xu and M. Yan, *Nano Energy*, 2014, **5**, 60-66.
58. F. C. Zheng, D. Q. Zhu and Q. W. Chen, *ACS Appl. Mater. Interfaces*, 2014, **6**, 9256-9264.
59. T. Brezesinski, J. Wang, R. Senter, K. Brezesinski, B. Dunn and S. H. Tolbert, *ACS Nano*, 2010, **4**, 967-977.
60. T. Brezesinski, J. Wang, J. Polleux, B. Dunn and S. H. Tolbert, *J. Am. Chem. Soc.*, 2009, **131**, 1802-1809.
61. Y. G. Li, P. Hasin and Y. Y. Wu, *Adv. Mater.*, 2010, **22**, 1926-1929.
62. C. F. Windisch, G. J. Exarhos, K. F. Ferris, M. H. Engelhard and D. C. Stewart, *Thin Solid Films*, 2001, **398**, 45-52.
63. V. Duffort, E. Talaie, R. Black and L. F. Nazar, *Chem. Mater.*, 2015, **27**, 2515-2524.
64. D. D. Yuan, X. H. Hu, J. F. Qian, F. Pei, F. Y. Wu, R. J. Mao, X. P. Ai, H. X. Yang and Y. L. Cao, *Electrochim. Acta*, 2014, **116**, 300-305.
65. I. Hasa, R. Verrelli and J. Hassoun, *Electrochim. Acta*, 2015, **173**, 613-618.
66. Z. Hong, K. Zhou, Z. Huang and M. Wei, *Sci. Rep.*, 2015, **5**, 11960-11970.
67. [Y. Xu](#), [M. Zhou](#), [L. Wen](#), [C. Wang](#), [H. Zhao](#), [Y. Mi](#), [L. Liang](#), [Q. Fu](#), [M. Wu](#) and [Y. Lei](#), *Chem. Mater.*, 2015, **27**, 4274-4280.



A soft templating approach enables facile synthesis of ordered mesoporous nickel cobaltite. These materials act as efficient anodes for high rate sodium ion batteries.